

## Fatigue characteristics of distributed sensing cables under low cycle elongation

Dan Zhang<sup>\*</sup>, Jiacheng Wang, Bo li and Bin Shi

*School of Earth Sciences and Engineering, Nanjing University, Nanjing 210023, P.R. China*

*(Received June 18, 2016, Revised September 30, 2016, Accepted October 2, 2016)*

**Abstract.** When strain sensing cables are under long-term stress and cyclic loading, creep may occur in the jacket material and each layer of the cable structure may slide relative to other layers, causing fatigue in the cables. This study proposes a device for testing the fatigue characteristics of three types of cables operating under different conditions to establish a decay model for observing the patterns of strain decay. The fatigue characteristics of cables encased in polyurethane (PU), GFRP-reinforced, and wire rope-reinforced jackets were compared. The findings are outlined as follows. The cable strain decayed exponentially, and the decay process involved quick decay, slow decay, and stabilization stages. Moreover, the strain decay increased with the initial strain and tensile frequency. The shorter the unstrained period was, the more similar the initial strain levels of the strain decay curves were to the stabilized strain levels of the first cyclic elongation. As the unstrained period increased, the initial strain levels of the strain decay curves approached those of the first cyclic elongation. The tested sensing cables differed in the amount and rate of strain decay. The wire rope-reinforced cable exhibited the smallest amount and rate of decay, whereas the GFRP-reinforced cable demonstrated the largest.

**Keywords:** distributed fiber optic sensing; strain sensing cable; fatigue; strain decay; low cycle elongation

### 1. Introduction

The progressive development of fiber optic communication, which entails using light to transmit signals, engendered fiber optic sensing technologies in the 1970s. Fiber optic cables are used as a medium for sensing and transmitting external signals. From 2000, distributed fiber optic sensing has been one of the fastest developing fiber optic sensing technologies (Bao and Chen 2012). Typical distributed fiber optic sensing technologies include optical time-domain reflectometry, Brillouin optical time-domain analysis (BOTDA), Brillouin optical time-domain reflectometry, and Brillouin optical frequency-domain analysis. Distributed fiber optic sensing involves executing a distributed measurement of specific optical fiber parameters (e.g., strain and temperature) by sensing the scattered light in the fibers. Thus, the sensing fibers can be embedded in reinforced concrete structures and geological bodies to conduct a long-term monitoring in the field of structural engineering (Ansari 2009, Li, Ou *et al.* 2015, Talebinejad, Fischer *et al.* 2009), geological engineering (Shi, Zhang *et al.* 2011), and others (Sun, Shi *et al.* 2014a, Feng, Wu *et al.*

---

<sup>\*</sup>Corresponding author, Associate Professor, E-mail: zhangdan@nju.edu.cn

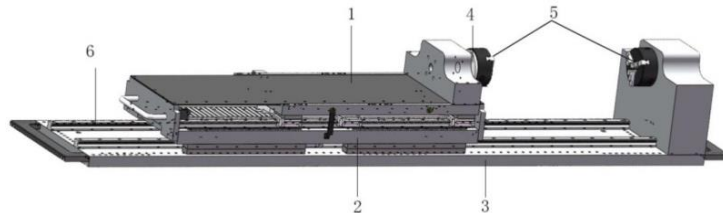
2015).

A typical optical fiber comprises multiple concentric layers: the core, cladding, and coating. Optical fibers composed of only the core and cladding layers are referred to as bare fibers. The material of a bare fiber (measuring 100-200  $\mu\text{m}$  in diameter) is silicon dioxide, which gives the fiber a high elastic modulus. The ultra-slim bare fiber can easily be damaged during installation and application. Thus, optical fibers are protected with a coating and jacket. The coating is made of silicone, whereas the jacket includes polymers such as nylon and polyvinyl chloride. Sensing cables are composed by wrapping the fiber in steel wires or metal-armored jackets, which improve the mechanical strength of the cables (Sun *et al.* 2014b). Fibers in distributed strain sensing cables should be tightly jacketed so that the cables can accurately measure the deformation of structures, rocks, or soil. However, sensing cables have complex structures and are composed of markedly different materials. Suhir and Bechou (2013) found that the fiber coating may share an appreciable fraction of the tensile load imparted to the coated fiber. Moreover, if the cables are under long-term stress, creep may occur in the jacket material and each layer of the cable structure may slide relative to other layers, consequently causing changes in the strain sensing performance of the cables (Ding, Shi *et al.* 2006, Iten 2011). Similar issues can also be found on the interface between an optical fiber coating and structural adhesives. The strain measurement accuracy that can be achieved by optical fiber sensors is highly based on the bonding characteristics of the various interface layers involved in the sensor bonding or embedding process (Brotzu, Felli *et al.* 2008).

Optical sensing fibers have been used for strain measurements and crack detection during structural damage tests (Chapeleau, Sedran *et al.* 2013, Hoult, Ekim *et al.* 2014, Wang, Han *et al.* 2014). Subject to cyclic loading and seasonal and diel temperature variations, the strain of sensing cables may fluctuate cyclically or change constantly, which is a major issue for distributed fiber optic sensing. The International Electrotechnical Commission (IEC) described five test methods for estimating the static fatigue parameters and dynamic fatigue parameters of optical fibers (IEC 60793-1-33 2001). The time to failure of an optical fiber under cyclic conditions may be calculated using power law theory (Evanoa, El Abdib *et al.* 2016, IEC/TR 62048 2001). As strain sensors, the mechanical reliability of optical fibers under water at different stresses was tested using a two-point bending method (El Shazly and Kukureka 2005). However, research on the strain sensing performance of fiber optic cables under long-term and cyclic loading has provided little evidence on whether cable performance changes as well as on the extent of performance-related changes. In general, the main manufacturer-provided mechanical specification of a cable is the maximum breakage force. Thus, investigating the fatigue characteristics of sensing cables under cyclic loading may have profound implications for the application and development of distributed fiber optic sensing.

To address this problem, this study presents a device for testing the tensile properties of distributed sensing cables and proposes a cyclic fatigue testing method. Through the application of this method, three sensing cables wrapped in different jackets were subjected to cyclic elongation to establish a decay model that reflected the strain decay pattern as the number of elongation cycles increased. The changes in the strain decay of the tested cables at different initial strain levels, tensile frequencies, and unstrained periods were examined to reveal the fatigue characteristics of these cables.

## 2. Testing



1. Linear motor, 2. linear motor panel, 3. grating ruler and read heads,  
4. force sensor, 5. three-jaw chuck, 6. rail panel

Fig. 1 Tensile testing device for distributed sensing cables

## 2.1 Apparatus

The tensile testing device for distributed sensing cables comprises a rail panel, linear motor panel, linear motor, grating ruler and read heads, electrical control cabinet, cables, force sensors, three-jaw chucks, and various other mechanical and electrical components. The linear motor panel, which is mounted on the rail panel, can be fixed at any position along the rail. The rail is 2 m long; thus, the testing device is applicable to cables shorter than 2 m. The linear motor can be moved within a maximum range of 405 mm on the linear motor panel. Thus, the testing device is applicable to cables with a maximum elongation of 405 mm. Two three-jaw chucks are fixed respectively on one end of the rail and one side of the linear motor to clamp a sensing cable for testing. The grating ruler, which is fixed on the lateral side of the rail panel, has two movable read heads, one of which is connected to the linear motor panel, and the other is connected to the linear motor. Both read heads were used to measure the relative movements of the linear motor panel and linear motor. The displacement, velocity, and acceleration of the linear motor were displayed and adjusted on a computer terminal. The motor driver features a force sensor, which measures the tensile properties of the cable. The data were displayed and processed on the computer terminal. Fig. 1 illustrates the structure of the tensile testing device for distributed sensing cables.

Before the fatigue characteristics of the sensing cables were tested, the position of the linear motor was fixed by adjusting its initial position according to the lengths of the cables and by threading the cables through the three-jaw chucks to secure them. During the testing process, sensors on the testing device returned the real-time parameters such as the displacement, velocity, and acceleration of the linear motor and the cable tensile properties to a computer that controlled the movement of the motor to test cable fatigue characteristics under different conditions.

The strain distributions of the three sensing cables were derived using a BOTDA system (NBX-6050A) (Zhang and Wu 2012), which had a spatial resolution of 5 cm, sampling interval of 1 cm, average number of  $2^{15}$ , and strain measurement accuracy of  $15 \mu\epsilon$  in this test.

## 2.2 Sensing cables

The fatigue characteristics of three sensing cables wrapped in polyurethane (PU), GFRP-reinforced, and wire rope-reinforced jackets were tested. Fig. 2 presents the structures of the sensing cables. Table 1 lists some parameters of the cables.

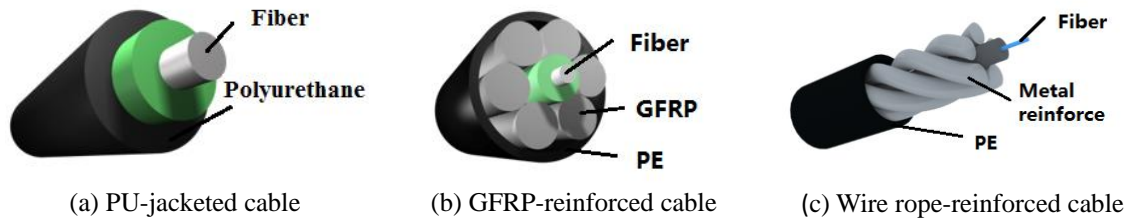


Fig. 2 Structures of the sensing cables

Table 1 Jackets and mechanical parameters of the sensing cables

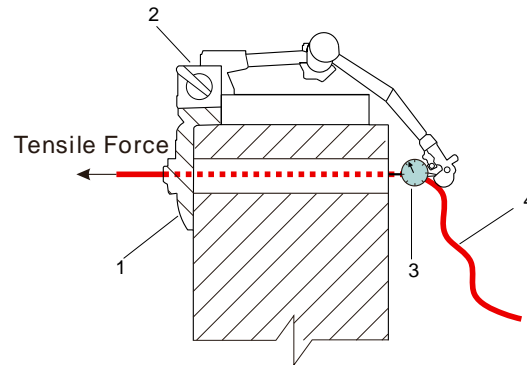
Jacket type	Cable diameter (mm)	Maximum tensile force (N)	Elastic module (GPa)
Polyurethane	2.0	220	0.2
GFRP-reinforced	5.8	1050	28
Wire rope-reinforced	5.0	2350	42

### 2.3 Testing procedure

Based on the actual operational conditions of the sensing cables, three tests were designed for cable fatigue characteristics: (1) an initial strain test, in which the cables were pre-elongated before installation; (2) a tensile frequency test, in which cyclic variations in the cable strain under vibration or temperature changes were examined; and (3) an unstrained period test, in which the cables were loose or unstrained. The temperature was controlled at  $23 \pm 2^\circ\text{C}$ , and relative humidity was maintained in the range of 45-55% for all tests.

All the tested cables measured 1 m in length. First, the cables were pre-elongated by moving the linear motor, engendering an initial deformation.. The immediate position of the motor was designated as its initial position. BOTDA was subsequently used to measure the initial strain ( $\varepsilon_0$ ) of the elongated segments of the cables ( $\varepsilon_0 \geq 1000 \mu\varepsilon$ ). Second, the initial strain was defined as the maximum strain. Reciprocating stretching was performed on the linear motor at frequencies of 3, 6, and 9 Hz with an amplitude of 1 mm. Thus, the strain ( $\mu\varepsilon$ ) of the cables varied in the range of  $[\varepsilon_0-1000, \varepsilon_0] \mu\varepsilon$ . Finally, the linear motor was returned to its initial position to measure the strain ( $\varepsilon$ ) of the cables after reciprocating stretching. Because the cables were clamped by the three-jaw chucks, with stress concentrations tending to occur on both ends of the cables, the average strain of the middle elongated cable segment (0.7 m in length) was used as the cable strain. During the testing, ambient temperature was recorded and temperature compensation was conducted for actual strain measurements.

To examine the clamping performance of the three-jaw chucks during the tests, the cables beyond the reach of the chucks were subjected to slight tension and affixed to a dial indicator (Fig. 3). Unchanged dial indicator readings during the tests indicated that the three-jaw chucks were highly effective in clamping the tested cables and that the strain variation of the tensile cable was not engendered by the loosening of the chucks.



1. Three-jaw chuck, 2. magnetic base, 3. dial indicator, 4. sensing cable

Fig. 3 Test on the clamping performance of the three-jaw chuck

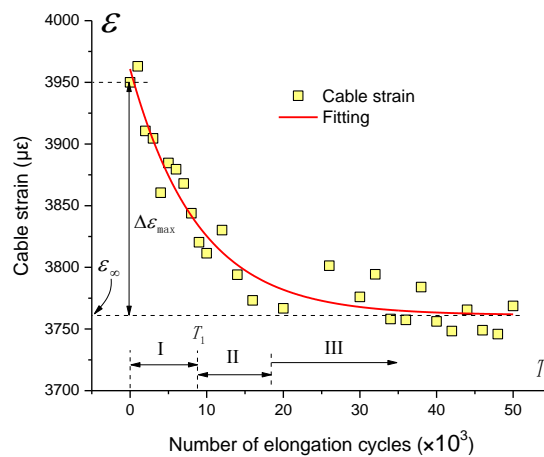


Fig. 4 Strain decay curve of the tested PU-jacketed sensing cable at a tensile frequency of 3 Hz

### 3. Fatigue characteristics of sensing cables

#### 3.1 Decay curve of cable strain

For every test, the cable should not be prestrained. In accordance with the aforementioned testing procedure, the initial strain ( $\epsilon_0$ ) of the PU-jacketed sensing cable was approximated as 4000  $\mu\epsilon$ . Cyclic elongation was executed at a tensile frequency of 3 Hz. The linear motor was returned to its initial position once every 1000 or 2000 cable elongation cycles, and the average strain of the tensile cable was subsequently measured using the BOTDA system. The preceding step was repeated to derive a strain decay curve of the PU-jacketed cable (Fig. 4); in this curve, the cable's strain decreased as the number of elongation cycles increased. The decay process of the cable's strain involved three stages. Stage I was the "quick decay" stage (the early phase of strain decay),

at which the cable's strain level declined rapidly and almost linearly. Stage II was the "slow decay" stage (the middle phase of strain decay), at which the cable's strain level exhibited a slow and nonlinear decline. Stage III was the "stabilization" stage (the late phase of strain decay), at which the cable's strain level stabilized and its strain decay peaked.

Fig. 4 indicates that the strain decay curve resembles an exponential function. Thus, curve fitting was performed using Eq. (1)

$$\varepsilon = \varepsilon_{\infty} + \Delta\varepsilon_{max} \cdot e^{\left(-\frac{T}{T_1}\right)} \quad (1)$$

where  $\varepsilon$  is the cable strain,  $T$  is the number of cable elongation cycles,  $\varepsilon_{\infty}$  is the strain level at the stabilization stage, and  $\Delta\varepsilon_{max}$  is the maximum decay of cable strain. Differentiating Eq. (1), with  $T = 0$ , yields the decay rate for  $T = 0$ , namely  $-\Delta\varepsilon_{max}/T_1$ . The cable strain decayed rapidly and almost linearly during the quick decay stage; thus,  $T_1$  was defined approximately as the number of elongation cycles at that stage ( $\times 10^3$ ). The fitting curve and parameters are presented in Fig. 4.

### 3.2 Decay characteristics of cable strain at different elongation frequencies

Based on tests of fatigue characteristics at a tensile frequency of 3 Hz, two other PU-jacketed cables were tested at the tensile frequencies of 6 and 9 Hz and the initial strain level of approximately 4000  $\mu\varepsilon$  to investigate the changes in the strain decay of the cables at these tensile frequencies. To minimize the effects of different initial strain levels on the results, the actual strain level was converted into a ratio of the strain level to the initial strain level under different numbers of elongation cycles, thus deriving standardized strain decay curves for the cables. Fig. 5 shows the standardized strain decay curves obtained at different tensile frequencies.

Eq. (1) was applied to perform fitting on the three standardized strain data sets to derive the characteristic parameters of the strain decay curve for the PU-jacketed sensing cable at different tensile frequencies (Table 2).

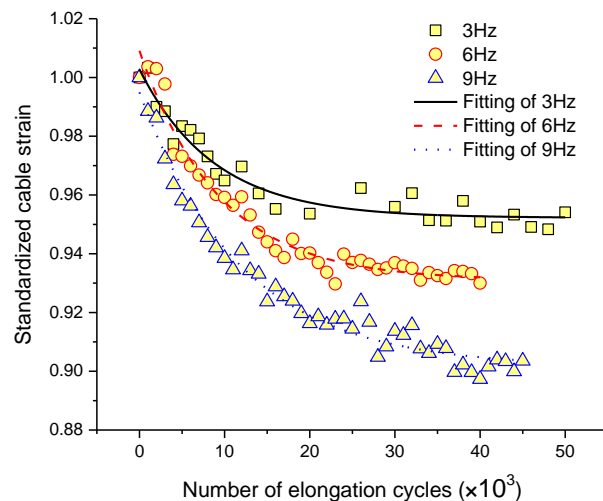


Fig. 5 Cable strain decay curves of the PU-jacketed cable at different tensile frequencies

Table 2 Characteristic parameters for the strain decay curves of the PU-jacketed sensing cable at different tensile frequencies

Tensile frequency (Hz)	$\epsilon_{\infty}$	$T$ ( $\times 10^3$ )	Standard deviation of $T$ ( $\times 10^3$ )	$\Delta\epsilon_{max}$	Decay rate at $T = 0$ ( $\times 10^{-5}$ )
3	0.952	8.809	1.117	0.051	0.574
6	0.931	9.311	0.704	0.078	0.840
9	0.902	11.888	0.784	0.093	0.786

Fig. 5 and Table 2 indicate consistent patterns of change in the strain decay curves at different tensile frequencies across the quick decay, slow decay, and stabilization stages. However, as the tensile frequency increased, three notable changes occurred: (1) The maximum amount of decay increased when the cable strain stabilized; (2) the number of elongation cycles required for completing the quick decay stage grew incrementally; and (3) the decay rates at  $T = 0$  for the 6- and 9-Hz strain decay curves were significantly higher than that for the 3-Hz curve.

### 3.3 Decay characteristics of cable strain under different initial strain conditions

To derive the strain decay curves under different initial strain conditions, the PU-jacketed sensing cable was subjected to cyclic elongation at initial strain levels of 1000, 4000, 6000, 8000, and 10000  $\mu\epsilon$ . Fig. 6 presents the results of the standardization of these curves. Eq. (1) was used to perform fitting on the standardized curves to derive the characteristic parameters of the curves (Table 3).

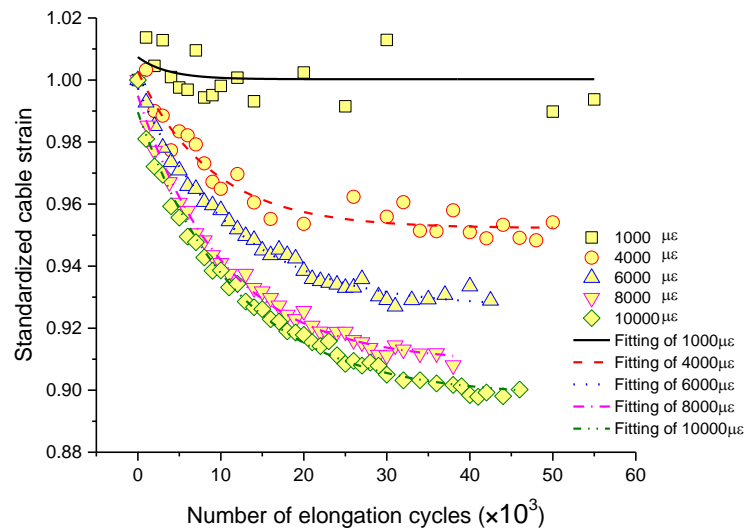


Fig. 6 Strain decay curves of the PU-jacketed sensing cable under different initial strain conditions

Table 3 Characteristic parameters for the strain decay curves of the PU-jacketed sensing cable at different initial strain levels

Initial strain/ $\mu\epsilon$	$\epsilon_{\infty}$	$T$ ( $\times 10^3$ )	Standard deviation of $T$ ( $\times 10^3$ )	$\Delta\epsilon_{max}$	Decay rate at $T$ = 0 ( $\times 10^{-5}$ )
1000	1.000	3.611	8.444	0.007	0.198
4000	0.952	8.809	1.117	0.051	0.574
6000	0.927	11.302	0.561	0.071	0.626
8000	0.909	10.455	0.436	0.086	0.824
10000	0.898	11.960	0.535	0.092	0.766

As indicated in Table 3, when the PU-jacketed sensing cable was at an initial strain level of 1000  $\mu\epsilon$ , with  $y_0 = 1.000$ , its strain level at the stabilization stage and its initial strain level were identical; thus, the cable showed no noticeable strain decay. In addition, when the cable strain was  $\geq 4000 \mu\epsilon$ , all the curves exhibited a consistent pattern of change. However, as the initial strain increased, the curves showed similar patterns to those at increased tensile frequencies: (1) The strain level declined gradually at the stabilization stage; that is, the amount of decay increased with the initial strain level; (2) the strain decay rate increased progressively at the quick decay stage overall; and (3) the number of elongation cycles required for completing the quick decay stage grew incrementally at the initial strain levels that were  $\leq 6000 \mu\epsilon$ , and this number did not change much at the initial strain levels that were  $> 6000 \mu\epsilon$ . According to the results presented in Sections 3.2 and 3.3, it can be concluded that the cable strain at high initial strain levels and tensile frequencies decayed at greater rates and in greater amounts.

### 3.4 Decay characteristics of cable strain at different unstrained periods

When a sensing cable is under long-term stress, creep may occur in its jacket material, and each layer of the cable structure may slide relative to the other layers. To investigate the resiliency of the cable strain decay, this study tested the fatigue characteristics of the PU-jacketed sensing cable at different periods. Each cable was subjected to initial cyclic elongation, after which the cable was relaxed in an unstrained state and idled sequentially for 1.5, 140, 1.5, 24, and 1.5 h. After each idling session was completed, the cable was subjected to a specific number of elongation cycles to derive strain decay curves for different idling periods (Fig. 7).

As the number of initial elongation cycles increased, the cable strain decayed and gradually stabilized. Because of the occurrence of plastic deformation in the cable material and relative sliding in each layer of the cable structure, the cable strain did not return to its initial level after both long (140 h) and short (1.5 h) idling periods. The stabilized strain levels for the long and short idling periods were approximately similar and lower than that of the first cyclic elongation. Moreover, comparing the results derived for the idling periods of 1.5, 24, and 140 h revealed that a longer the unstrained period was, the closer the initial strain levels of the strain decay curves were to those of the first cyclic elongation. For the idling period of 1.5 h, the initial strain levels of strain decay curves were even closer to the stabilized strain levels under the first cyclical elongation, indicating that the cable did not recover completely from fatigue after it had been idled for a short

period. Notably, the results from the three short idling periods suggested that the strain decay curves, decay rates, and stabilized strain levels for all the short idling periods exhibited almost identical changes. Specifically, the resiliency of the strain decay depended on the idling periods instead of the idling history.

#### 4. Strain decay curves of different sensing cables

Fig. 8 illustrates the strain decay curves of the sensing cables with GFRP-reinforced and wire rope-reinforced jackets at different tensile frequencies and an initial strain level of  $4000 \mu\epsilon$ . Table 4 presents the characteristic parameters for these curves. The curves exhibited patterns of change consistent with those of the PU-jacketed sensing cable: (1) The cable strain changed across the quick decay, slow decay, and stabilization stages; and (2) when the cable strain stabilized, the maximum decay increased with the tensile frequency. However, the pattern of change observed for the GFRP-reinforced sensing cable differed from that observed for the wire rope-reinforced sensing cable. Under the same conditions (namely initial strain, tensile frequency, and unstrained period), the maximum decay of the GFRP-reinforced cable was significantly higher than those of the wire rope-reinforced and PU-jacketed cables. The number of elongation cycles required for completing the quick decay stage was higher for the GFRP-reinforced cable than for the wire rope-reinforced cable. In addition, the wire rope-reinforced cable had the smallest decay rate at  $T = 0$ .

Fig. 9 presents the strain decay curves of the GFRP-reinforced and wire rope-reinforced strain sensing cables under different initial strain conditions, and Table 5 shows the characteristic parameters for these curves. As the number of elongation cycles increased, the strain of the cables gradually decayed through the quick decay, slow decay, and stabilization stages. The maximum decay of both cables increased with the initial strain level. Notably, at the same initial strain levels, the maximum decay and the decay rate at  $T = 0$  of the GFRP-reinforced cable were significantly greater than those of the wire rope-reinforced cable.

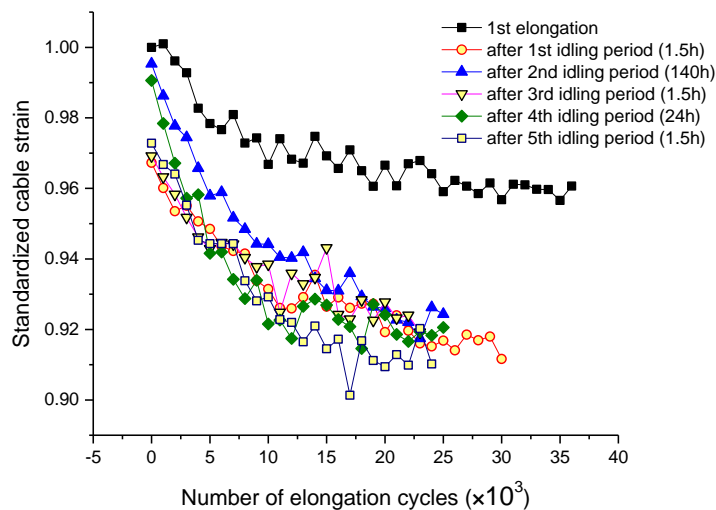


Fig. 7 Strain decay curves of the PU-jacketed cable for different idling periods

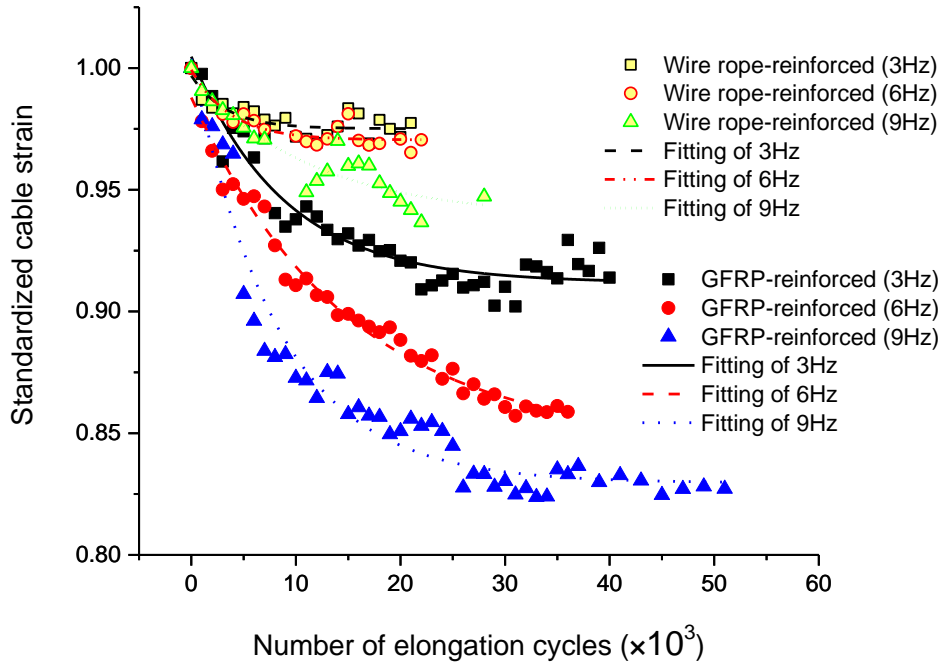


Fig. 8 Strain decay curves of GFRP-reinforced and wire rope-reinforced strain sensing cables at different tensile frequencies

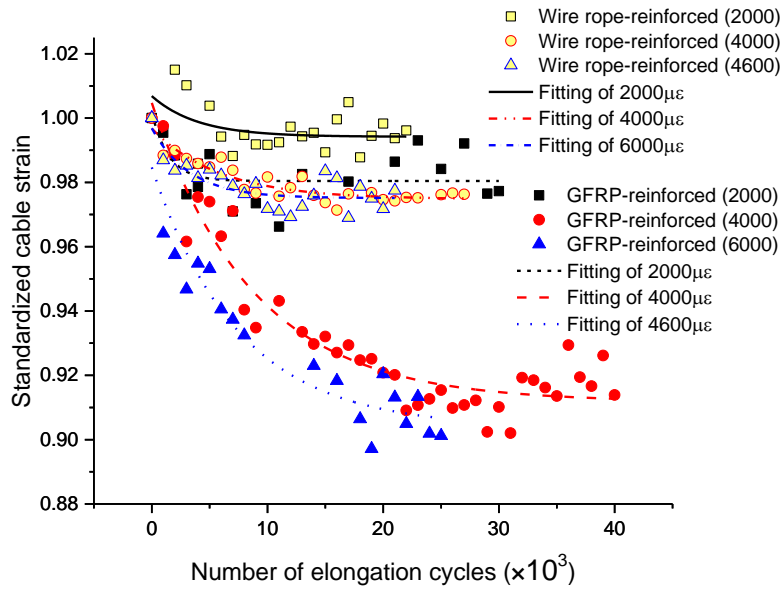


Fig. 9 Strain decay curves of GFRP-reinforced and wire rope-reinforced strain sensing cables at different initial strain levels

Table 4 Characteristic parameters for the strain decay curves of GFRP-jacketed and wire rope-jacketed strain sensing cables at different tensile frequencies

Cable type	Tensile frequency	$\varepsilon_{\infty}$	$T$ ( $\times 10^3$ )	Standard deviation of $T$ ( $\times 10^3$ )	$\Delta\varepsilon_{max}$	Decay rate at $T = 0$ ( $\times 10^{-5}$ )
GERP-reinforced	3 Hz	0.912	8.786	1.040	0.093	1.058
	6 Hz	0.845	14.937	1.208	0.142	0.953
	9 Hz	0.830	8.240	0.631	0.174	2.114
Wire rope-reinforced	3 Hz	0.975	5.916	1.245	0.022	0.371
	6 Hz	0.970	3.723	0.905	0.029	0.775
	9 Hz	0.939	11.590	4.232	0.058	0.501

Table 5 Characteristic parameters for the strain decay curves of GFRP-jacketed and wire rope-jacketed sensing cables at different initial strain levels

Cable type	Initial strain	$\varepsilon_{\infty}$	$T$ ( $\times 10^3$ )	Standard deviation of $T$ ( $\times 10^3$ )	$\Delta\varepsilon_{max}$	Decay rate at $T = 0$ ( $\times 10^{-5}$ )
GFRP-reinforced	2000	0.980	1.504	1.142	0.021	1.413
	4000	0.912	8.786	1.040	0.093	1.058
	6000	0.904	7.539	1.814	0.081	1.073
Wire rope-reinforced	2000	0.994	3.978	3.810	0.013	0.318
	4000	0.975	5.916	1.245	0.022	0.371
	4600	0.975	3.286	1.159	0.022	0.662

### 5. Conclusions

Given the lack of methods for comprehensively examining the performance of sensing cables under cyclic loading, this study presents a tensile testing device for strain sensing cables and proposes a cyclic fatigue testing method. PU-jacketed, GFRP-reinforced, and wire rope-reinforced sensing cables were subjected to fatigue testing to yield their respective fatigue characteristics at various initial strain levels, tensile frequencies, and unstrained periods.

The study findings are outlined as follows. First, the cable strain gradually decayed as the number of elongation cycles increased; thus, the strain decay curve corresponded to an exponential decay model under which the decay process was divided into quick decay, slow decay, and stabilization stages. Second, the strain decay increased with the initial strain and tensile frequency. Third, the shorter the unstrained period was, the more similar the initial strain levels of the strain decay curves were to the stabilized strain levels of the first cyclic elongation. In addition, as the unstrained period increased, the initial strain levels of the strain decay curves approached those of initial cyclic elongation. Fourth, sensing cables with different jackets differed in the amount and

rate of decay; under the same conditions, the wire rope-reinforced cable exhibited the smallest amount of decay whereas the GFRP-reinforced cable demonstrated the largest.

In sum, the proposed cyclic fatigue testing method can be used to identify the fatigue characteristics of distributed strain sensing cables with different jackets and can serve as a reference in assessments of cable performance during long-term use.

## Acknowledgments

The authors gratefully acknowledge the financial support provided by the National Natural Science Foundation of China (41272315, 41572271) and the State Key Program of National Natural Science of China (41427801).

## References

- Ansari, F. (2009), "Structural health monitoring with fiber optic sensors", *Frontiers of Mechanical Engineering in China*, **4**(2), 103-110.
- Bao, X.Y. and Chen, L. (2012), "Recent progress in distributed fiber optic sensors", *Sensors*, **12**(7), 8601-8639.
- Brotzu, A., Felli, F. and Fiori, L. (2008), "Characterization of both adhesion and interfacial interaction between optical fiber coating and structural adhesives", *Smart Struct. Syst.*, **4**(4), 439-448.
- Chapeleau, X., Sedran, T. and Cottineau, L.M. (2013), "Study of ballastless track structure monitoring by distributed optical fiber sensors on a real-scale mockup in laboratory", *Eng. Struct.*, **56**, 1751-1757.
- Ding, Y., Shi, B. and Bao, X. (2006), "Jacket effect on strain measurement accuracy for distributed strain sensors based on Brillouin scattering", *Optica Applicata*, **36**(1), 57-67.
- El Shazly, Y.M. and Kukureka, S.N. (2005), "Mechanical reliability of optical fibre for strain sensors", *Proceedings of the SPIE Vol. 5855, 17th International Conference on Optical Fibre Sensors*, Bruges, Belgium, May.
- Evanoa, N., El Abdib, R. and Poulain, M. (2016), "Lifetime modeling of silica optical fiber in static fatigue test", *J. Appl. Res. Technol.*, **14**, 278-285.
- Feng, X., Wu, W.J. and Li, X.Y. (2015), "Experimental investigations on detecting lateral buckling for subsea pipelines with distributed fiber optic sensors", *Smart Struct. Syst.*, **15**(2), 245-258.
- Hoult, N.A., Ekim, O. and Regier, R. (2014), "Damage/Deterioration detection for steel structures using distributed fiber optic strain sensors", *J. Eng. Mech. - ASCE*, **140**(12), 04014097.
- IEC 60793-1-33 (2001), Optical fibers - Part 1-33: Measurement methods and test procedures - Stress corrosion susceptibility, International Electrotechnical Commission: Switzerland.
- IEC/TR 62048 (2011), Optical fibres - Reliability - Power law theory, International Electrotechnical Commission, Switzerland.
- Iten, M. (2011), "Novel applications of distributed fiber optic sensing in geotechnical engineering", Ph.D. Dissertation, ETH Zurich, Zurich.
- Li, H., Ou, J. and Zhang, X. (2015), "Research and practice of health monitoring for long-span bridges in the mainland of China", *Smart Struct. Syst.*, **15**(3), 555-576.
- Shi, B., Zhang, D. and Zhu, H.H. (2011), "Application of distributed optical fiber strain measurement into geotechnical engineering monitoring", *Proceedings of the 8th International Workshop on Structural Health Monitoring*, Stanford, USA, September.
- Suhir, E. and Bechou, L. (2013), "Saint-Venant's principle and the minimum length of a dual-coated optical fiber specimen in reliability (proof) testing", *Microelectronics Reliability*, **53**(9-11), 1506-1509.
- Sun, Y.J., Shi, B. and Chen, S.E. (2014a), "Feasibility study on corrosion monitoring of a concrete column

- with central rebar using BOTDR”, *Smart Struct. Syst.*, **13**(1), 41-53.
- Sun, Y.J., Zhang, D. and Shi, B. (2014b), “Distributed acquisition, characterization and process analysis of multi-field information in slopes”, *Eng. Geol.*, **182**(Part A), 49-62.
- Talebinejad, I., Fischer, C. and Ansari, F. (2009), “Serially multiplexed FBG accelerometer for structural health monitoring of bridges”, *Smart Struct. Syst.*, **5**(4), 345-355.
- Wang, L.C., Han, J.G. and Song, Y.P. (2014), “Fatigue performance monitoring of full-scale PPC beams by using the FBG sensors”, *Smart Struct. Syst.*, **13**(6), 943-957.
- Zhang, H. and Wu, Z.S. (2012), “Performance Evaluation of PPP-BOTDA-Based Distributed Optical Fiber Sensors”, *Int. J. Distributed Sensor Networks*, **2012**, 1-12.

*BS*